Chemical Engineering Science 311 (2025) 121575

Contents lists available at ScienceDirect

Chemical Engineering Science

journal homepage: www.elsevier.com/locate/ces

Model-based description of droplet deformation into polyhedral shapes in liquid-liquid polydisperse dense-packed zones

Stepan Sibirtsev, Lukas Thiel, Yannik Danner, Andrey Kirsanov, Andreas Jupke*

Fluid Process Engineering (AVT.FVT), RWTH Aachen University, Forckenbeckstraße 51, 52074, Aachen, Germany

ARTICLE INFO

Keywords:
Dense-packed zones
Liquid-liquid phase separation
Droplet deformation
Bond number correlation

ABSTRACT

Droplet deformation in liquid-liquid dense-packed zones (DPZs) significantly impacts the dispersed phase volume fraction and droplet coalescence, which is crucial to phase separation processes in various industrial equipment. This study introduces a modeling approach to describe droplet deformation into polyhedral shapes in polydisperse DPZs. Droplet deformation, characterized by the contact radius r_f, the curvature radius r_a, and the volume ratio ε_i is modeled using equations based on pressure, geometric, and volumetric relationships for regular polyhedra as well as Bond number correlations. Moreover, generalized Bond number correlations are proposed to extend the approach to irregular convex polyhedral shapes. Simulations across technical Bond number ranges demonstrate that r_f and ε_i increases with the Bond number, while r_a decreases, approaching zero at high Bond numbers. The Bond number correlations strongly agree with equation-based solutions, with mean absolute percentage errors below 3.0 %. Practical implications include enhanced predictions for DPZ behavior and integration into a common coalescence model.

1. Introduction

The deformation of droplets in liquid-liquid dense-packed zones (DPZ) affects the volume fraction of the dispersed phase within the DPZ (Henschke, 1995; Lacasse et al., 1996; Abe and Inasawa, 2022; Sibirtsev et al., 2025) as well as the droplet coalescence (Henschke, 1995, 2002; Chan et al., 2011; Bozzano and Dente, 2010). Both the dispersed phase volume fraction and droplet coalescence significantly impact the formation and dissolution of the DPZ, thereby influencing the phase separation behavior of liquid-liquid dispersions (Henschke, 1995, 2002; Thaker and Buwa, 2019; Steinhoff et al., 2018).

Since DPZs are encountered in various types of equipment used for liquid-liquid phase separation processes - such as batch-settling cells (Henschke, 1995; Sibirtsev et al., 2024; Leleu and Pfennig, 2019; Sibirtsev et al., 2019), stirred and sieve tray columns (Weber and Jupke, 2020; Sovilj et al., 2019; Graham et al., 1979; Mohanty and Vogelpohl, 1997), vertical and horizontal gravity settlers (Rommel et al., 1992; Frising et al., 2006; Schlieper et al., 2004; Ye et al., 2023b; Steinhoff et al., 2021), batch stirred tanks (Ye et al., 2023a), and centrifugal extractors (Eggert et al., 2019) - an accurate, model-based description of droplet deformation, and consequently the DPZ, is essential for the proper design of such equipment.

Henschke (1995) developed a model to describe droplet deformation within the DPZ, which has been successfully applied to batch-settling cells (Henschke, 2002; Leleu and Pfennig, 2019; Eberz et al., 2025), horizontal gravity settlers (Henschke, 1995; Schlieper et al., 2004), and batch stirred tanks (Ye et al., 2023a). However, this model assumes that the DPZ is formed by a monodisperse droplet size distribution (Henschke, 1995). This assumption limits the level of detail in the deformation modeling, potentially leading to an underestimation of the DPZ height (Henschke, 1995), and thus, an increased risk of apparatus flooding.

In technical applications, the DPZ is typically formed by a polydisperse droplet size distribution (Thaker and Buwa, 2019; Thaker et al., 2018; Raynel et al., 2023). Therefore, improving the accuracy of DPZ height predictions requires increasing the level of detail in deformation modeling by accounting for polydispersity.

This study introduces a modeling approach for droplet deformation into polyhedral shapes, accounting for the polydispersity of the DPZ. The approach is based on pressure, geometrical, and volumetric relationships generally applicable to regular polyhedral shapes: tetrahedron, cube, octahedron, dodecahedron, and icosahedron. These polyhedral shapes are characteristic for random loose packings of polydisperse, deformed droplets (Sibirtsev et al., 2025). Furthermore, generalized semi-empirical correlations based on the Bond number (Bo) are proposed to describe the deformation of droplets into both regular and irregular convex polyhedral shapes.

* Corresponding author.
E-mail address: andreas.jupke@avt.rwth-aachen.de (A. Jupke).

https://doi.org/10.1016/j.ces.2025.121575
Received 11 January 2025; Received in revised form 16 March 2025; Accepted 21 March 2025
Available online 25 March 2025

Nomenclature

a	Edge length of the polyhedron
a_0	Initial guess for the edge length
a_{max}	Maximum edge length
a_{min}	Minimum edge length
A_j	Value of the iterative solution
A_a	Area of the circular segment
A_c	Channel area
A_f	Contact area between droplets
A_p	Polyhedral face area
A_s	Intersection area
A_t	Area of an isosceles triangle
Bo	Bond number
b	Polyhedron edge
C_A	Polyhedral shape constant
C_{cor}	Correction factor
C_{rc}	Polyhedral shape constant
C_{rm}	Polyhedral shape constant
C_{rs}	Polyhedral shape constant
C_V	Polyhedral shape constant
C_j	Fitting parameter
$E_{L,j}$	Results of the left hand side equation
$E_{R,j}$	Results of the right hand side equation
h_{eq}	Equivalent DPZ height
h_i	Height of the DPZ acting on the droplet
$MAPE_j$	Mean absolute percentage error
N_c	Number of polyhedron corners
N_E	Number of equations
N_e	Number of polyhedron edges
N_{fc}	Number of polyhedron's face corners
N_p	Number of fitted points
N_r	Number of calculation results
p_i	Pressure acting on the droplet i
p_d	Excess pressure inside the droplet
p_{eq}	Equivalent pressure
p_f	Pressure acting on the contact area between droplets
$\bar{p}_f$	Pressure at all deformation stages
$p_{f,max}$	Maximum pressure acting on the contact area between droplets
$p_{f,min}$	Minimum pressure acting on the contact area between droplets
p_h	Hydrostatic pressure
p_{in}	Pressure inside the droplet
p_{out}	Pressure outside the droplet
$p_{out,c}$	Pressure outside the droplet in the center of the drainage film
$p_{out,r}$	Pressure outside the droplet behind the rim
p_s	Excess pressure within the drainage film
P_j	Predicted values by the Bond number correlation
P	Intersecting point
p	Pressure
r_a	Radius of droplet's curvature regions
$r_{a,0}$	Initial guess for the curvature radius
$r_{a,max}$	Maximum curvature radius
$r_{a,min}$	Minimum curvature radius
r_c	Incircle radius of the polygon representing the polyhedron's face
r_{eq}	Equivalent droplet radius
r_f	Radius of the contact areas between droplets
$r_{f,0}$	Initial guess for the contact area radius
$r_{f,max}$	Maximum contact area radius
$r_{f,min}$	Minimum contact area radius
r_o	Incircle radius of contact area's polygon
r_s	Polyhedron's insphere radius
V_c	Channel volume
V_p	Polyhedron volume
V	Droplet's volume
x	Distance between point P and the polygon border
y	Polyhedron edge length
α	Half the angle between two polyhedron faces
$\bar{\varepsilon}_p$	Average volume fraction of the dispersed phase in the DPZ
$\varepsilon_{i,max}$	Maximum volume fraction
$\varepsilon_{i,min}$	Minimum volume fraction
ε_i	Volume fraction
δ	Triangle angle
$\Delta\rho$	Density difference between the two liquid phases
σ	Interfacial tension
Ψ	Substitution

2. Fundamentals

The degree of droplet deformation within a DPZ is governed by the interplay between the buoyancy force exerted by the DPZ and the deformation resistance of the droplets, which is determined by interfacial tension (Henschke, 1995). Deformation leads to the formation of plane contact areas between droplets and regions of curvature, ultimately shaping the droplets into polyhedral structures (Lacasse et al., 1996; Abe and Inasawa, 2022; Thaker and Buwa, 2019; Höhler and Weaire, 2019). While the exact deformation shape can be predicted using Morse-Witten theory (Morse and Witten, 1993), this method is computationally intensive (Höhler and Weaire, 2019; Dunne et al., 2019).

However, knowledge of the exact deformation shape is not required to determine the volume fraction of the dispersed phase or droplet coalescence within the DPZ, which is critical for the formation and dissolution of the DPZ. To address this, Henschke (1995) proposed a less computationally intensive model that assumes a monodisperse droplet size distribution forms the DPZ and that the droplets deform into a dodecahedron shape. The model is based on an equation system involving pressure, geometrical, and volumetric relationships and is solved iteratively. In Henschke's model, droplet deformation is characterized by two radii: r_f, which represents the radius of the contact areas between droplets, and r_a, which describes the radius of droplet's curvature regions. Moreover, the edge length a of the polyhedron is a required parameter to determine r_f and r_a.

In addition to the equation system, Henschke introduced semi-empirical Bo number correlations. During deformation, the gravitational and interfacial tension forces act on the droplet's interface. While the gravitational force favors deformation, the interfacial tension force counteracts deformation. The resulting equilibrium of forces determines the degree of deformation. The Bo number represents the ratio of gravitational force to interfacial tension force and, thus, is suitable for a model-based description of droplet deformation. The Bo number correlations are fitted to the results of the iterative solution of the equation system and, while less computationally intensive, effectively captures the dependence of r_f, r_a on the relevant influencing parameters (Henschke, 1995). Furthermore, Henschke proposed a model for calculating droplet coalescence within the DPZ based on r_f and r_a (Henschke, 1995, 2002).

However, the derivation of the deformation model (Henschke, 1995) is partially challenging to interpret and limited to the dodecahedron shape. Moreover, the source of the derivation is written in German,

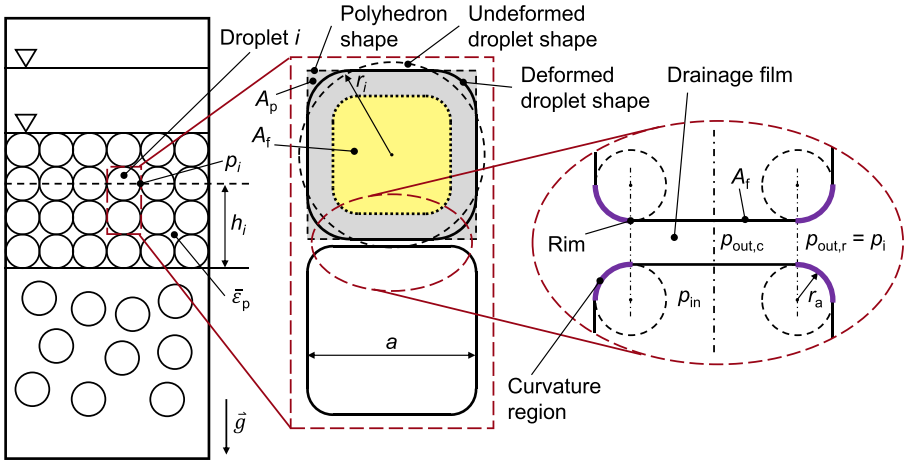

Fig. 1. Relevant parameters during the droplet deformation of two equal-sized droplets into a cubic shape.

which makes it less internationally accessible. A later publication (Henschke, 2002), written in English, aimed to present the model but introduced equations that conflict with the original source (Henschke, 1995) and are mathematically inappropriate for describing certain relationships. For example, the equation proposed for the asymptotically decreasing curve of r_a (Henschke, 2002) fails to accurately reflect the mathematical behavior described in the original work (Henschke, 1995).

In technical applications, the DPZ is typically formed by a polydisperse droplet size distribution (Thaker and Buwa, 2019; Thaker et al., 2018; Raynel et al., 2023). This polydispersity leads to the formation of various polyhedral shapes during droplet deformation. The deformation shape in a polydisperse DPZ is influenced by the droplet's contact number, representing the number of neighboring droplets in contact with a given droplet (Sibirtsev et al., 2025; Liu et al., 2019).

Sibirtsev et al. conducted a model-based study on droplet contact numbers in liquid-liquid DPZs formed by log-normal and Gaussian droplet size distributions (Sibirtsev et al., 2025). Their findings indicate that the contact number of droplets can range from 4 to 65, depending on the droplet size distribution's shape and the droplet class's diameter. Additionally, their study identified five regular polyhedral shapes commonly occurring in DPZs: tetrahedron, cube, octahedron, dodecahedron, and icosahedron.

3. Modeling

This study aims to develop a modeling approach for droplet deformation into polyhedral shapes that accounts for DPZ polydispersity and characterizes deformation using r_f, r_a, and the volume ratio ε_i between the droplet's volume and the volume of its corresponding polyhedral shape. This approach enables the straightforward integration of the new deformation model into the droplet coalescence model proposed by Henschke (1995, 2002). The modeling approach is derived in a generalized form applicable to all regular polyhedral shapes, building upon the foundational principles of Henschke's deformation model (Henschke, 1995).

Furthermore, generalized semi-empirical correlations based on the *Bo* number are proposed to describe droplet deformation into regular and irregular convex polyhedral shapes with an uniform edge length a. It is assumed that the deformation behavior of droplets into regular and irregular convex polyhedral shapes with an uniform edge length a is comparable. Consequently, the insights gained from modeling droplet deformation into regular polyhedral shapes can be applied to the deformation of droplets into these irregular convex shapes.

In addition, it is assumed that the density difference $\Delta\rho$ between the two liquid phases, the interfacial tension σ, the average volume fraction $\bar{\varepsilon}_p$ of the dispersed phase in the DPZ and the height h of the DPZ acting on the droplet are known material system and operating parameters, or are obtained from established models (Henschke, 1995, 2002; Leleu and Pfennig, 2019).

The typical geometric relationships for polyhedra, polygons, and spheres used in this study are documented in Bronshtein (2007). The deduced geometric and volumetric relationships are generalized for regular polyhedral shapes by incorporating polyhedral shape-dependent constants C_p, which are listed in the supporting information (SI) Tab. 1 and include C_A, C_{rc}, C_{rm}, C_V, and C_{rs}.

According to the droplet deformation model proposed by Henschke (1995, 2002), the degree of deformation of a droplet i is characterized by the radii r_f and r_a as well as the edge length a. Since r_f, r_a, and a are unknown, a system of three equations is required to establish the connection between these parameters and the deformation conditions. The pressure relationship, geometric relationship, and volumetric relationship define these equations.

3.1. Pressure relationship

Fig. 1 illustrates the relevant parameters involved in droplet deformation, exemplified for two equal-sized droplets deformed into a cubic shape. Additionally, the contact area A_f between the droplets is highlighted in yellow, while the curvature regions are highlighted in violet.

Each droplet i within the DPZ experiences a pressure p, generated by the buoyancy force exerted by the DPZ droplets affecting droplet i. This pressure drives the deformation of the droplets and is defined by Eq. (1), where g is the gravitational constant.

$$p = \Delta\rho g \bar{\varepsilon}_p h \tag{1}$$

Since the droplets deform from a spherical shape into a polyhedral shape, p acts on each polyhedral face area A_p. The area A_p is dependent on the specific polyhedral shape and is generally determine by Eq. (2).

$$A_p = C_A a^2 \tag{2}$$

According to Henschke, the contact area A_f does not form a perfect circle but rather a polygonal shape corresponding to the polyhedron's face, with rounded corners (Henschke, 1995). However, Henschke's coalescence model employs the radius r_f, which is derived from A_f using Eq. (3). Here, r_f represents the radius of a circle with an area equal to A_f, approximating the polygon.

$$A_f = \pi r_f^2 \tag{3}$$

The pressure p_f acting on the contact area A_f is related to the pressure p and the area A_p according to Eq. (4) (Henschke, 1995).

$$p_f A_f = p A_p \tag{4}$$

The pressure $p_f = p_{in} - p_{out}$ arises from the pressure difference between the pressure inside the droplet $p_{in} = p_h + p + p_d$ and the pressure outside the droplet $p_{out} = p_h + p + p_s$. Here, p_h is the hydrostatic pressure, p_d is the excess pressure inside the droplet relative to its bulk phase, as described by the Young-Laplace equation (de Gennes et al., 2004), and p_s is the excess pressure within the drainage film between the droplets, resulting from the droplets being pushed together.

The pressure difference between p_{in} and p_{out} drives the formation of curvature regions with the radius r_a. Thus, r_a is related to this pressure difference by the Young-Laplace equation, as shown in Eq. (5) (Henschke, 1995).

$$p_f = p_{in} - p_{out} = \frac{2\sigma}{r_a} \tag{5}$$

Moreover, the pressure outside the droplet, p_{out}, depends on the location considered. Behind the rim of the droplet, $p_s = 0$, and p_{out} reaches its minimum value, $p_{out} = p_{out,r}$, which is equal to $p_{out,r} = p_h + p$. In the center of the film, p_{out} reaches its maximum value, $p_{out} = p_{out,c}$. The increase in pressure from the rim to the center is approximated according to Eq. (6) (Chen et al., 1984).

$$p_{out,c} = p_{out,r} + \frac{\sigma}{r_a} = p_h + p + \frac{\sigma}{r_a} \tag{6}$$

Further, Eq. (5) is considered at two boundary deformation stages. When the DPZ height affecting the droplet is approaching zero, no deformation occurs ($p \to 0$, $p_s \to 0$) and p_{out} becomes independent of the considered location reaching its minimum value, which is equal to p_h in this case (Abid and Chesters, 1994). At this deformation stage, the radius of the droplet's curvature regions approaches the droplet's radius with $r_a \to r$ (Henschke, 1995), and Eq. (5) results in Eq. (7).

$$p_{f,min} = p_d = \frac{2\sigma}{r_a} \tag{7}$$

When $p \to \infty$, maximum deformation is reaching and p_{out} approaches its maximum value of $p_{out} \to p_{out,c}$ according to Eq. (6). At this deformation stage, the droplet's volume becomes almost equivalent to the polyhedron volume with $r_a \to 0$ (Henschke, 1995), and Eq. (5) results in Eq. (8).

$$p_{f,max} = p_d - \frac{\sigma}{r_a} = \frac{\sigma}{r_a} \tag{8}$$

To describe the pressure p_f at all deformation stages from $p \to 0$ to $p \to \infty$, Henschke proposed Eq. (9).

$$\bar{p}_f = \frac{2\sigma}{r_a\left(2 - \frac{r_a}{r}\right)} \tag{9}$$

Combining the introduced equations, the pressure relationship is represented by Eq. (10). Since $\Delta\rho$, $\bar{\varepsilon}_p$, and h are assumed to be known parameters, p is a known parameter (Eq. (1)). The resulting pressure relationship is similar to the one proposed by Henschke (1995) but is derived from the participating pressures more precisely in this work.

$$\pi r_f^2 \frac{2\sigma}{r_a\left(2 - \frac{r_a}{r}\right)} = C_A a^2 p \tag{10}$$

3.2. Geometric relationship

Although r_f, r_a, and a are dependent on the specific polyhedral shape, a general geometric relationship connects them through the intersection area A_s and the polyhedron face area A_p. Fig. 2 illustrates this geometric relationship, exemplified by the tetrahedron shape, and is used to derive the general relationship. In Fig. 2a, the intersection area A_s (in blue) is perpendicular to the polyhedron edge b and intersects the point P located at the center of b. Thus, A_s passes through the center of the polygon corresponding to the contact areas A_f (in yellow) located at the face areas A_p. The shapes of A_s and A_p depend on the polyhedron's shape. However, the location of A_s is defined by the polyhedron edge b and point P shape-independent. In Fig. 2b and c, the areas A_p and A_s are illustrated, respectively. Additionally, all relevant polyhedral shape parameters involved in droplet deformation and the shape of the deformed droplet (in green) are shown.

The area A_f is approximated by a polygon with angular corners (Fig. 2b) according to Eq. (11), where y is the polygon edge length.

$$A_f = C_A y^2 \tag{11}$$

The edge length y is related to the incircle radius r_o of this polygon according to Eq. (12).

$$y = \frac{r_o}{C_{rc}} \tag{12}$$

The relationship in Eqs. (11) and (12) matches the boundary condition at $p \to \infty$, since at this condition $r_o \to r_c$, $y \to a$, and thus, $A_f \to A_p$, with r_c as the incircle radius of the polygon representing the polyhedron's face A_p. Moreover, the boundary condition at $p \to 0$ is matched, since at this condition $r_o \to 0$, $y \to 0$, and thus, $A_f \to 0$.

Furthermore, the radius r_o and the parameters r_a and a are geometrically connected through the incircle radius r_c. The radius r_c is determined according to Eq. (13).

$$r_c = C_{rc} a \tag{13}$$

In addition, r_c is determined by the degree of deformation and thus connected to the radius r_o according to Eq. (14), where x is the distance between point P and the polygon border of the contact area A_f.

$$r_c = r_o + x \tag{14}$$

The distance x is determined according to Eq. (15), where α is half the angle between two polyhedron faces.

$$x = \frac{r_a}{\tan(\alpha)} \tag{15}$$

According to Eq. (16), the angle α is expressed by the radius r_c (Eq. (13)) and the polyhedron's midsphere radius $r_m = C_{rm} a$.

$$\alpha = \arccos\left(\frac{r_c}{r_m}\right) = \arccos\left(\frac{C_{rc}}{C_{rm}}\right) \tag{16}$$

Combining the introduced equations the general geometric relationship is represented by Eq. (17). Compared to the geometric relationship proposed by Henschke (1995), the presented relationship is explicit and requires no correction factors.

$$\left(\frac{\pi C_{rc}^2}{C_A}\right)^{1/2} r_f + \frac{r_a}{\tan\left(\arccos\left(\frac{C_{rc}}{C_{rm}}\right)\right)} = C_{rc} a \tag{17}$$

3.3. Volumetric relationship

Although the volume of the deformed droplet depends on the polyhedral shape, it is described by a general volumetric relationship. Fig. 2 illustrates this volumetric relationship, exemplified by the tetrahedron shape, and is used to deduce the general relationship. As proposed by Henschke (1995), the volume of the deformed droplet is approximated by subtracting the channel volume V_c (in orange) of the curvature region from the polyhedron volume V_p. Moreover, due to the conservation of mass, the resulting volume of the deformed droplet is equal to the volume V of the undeformed droplet, as given by Eq. (18), where N_e is the number of polyhedron edges according to SI Tab. 1.

$$V = V_p - N_e V_c \tag{18}$$

The volume of the undeformed droplet is given by $V = \frac{\pi}{6} d^3$, with $d = 2r$ as the equivalent droplet diameter. The polyhedron volume is determined according to Eq. (19).

$$V_p = C_V a^3 \tag{19}$$

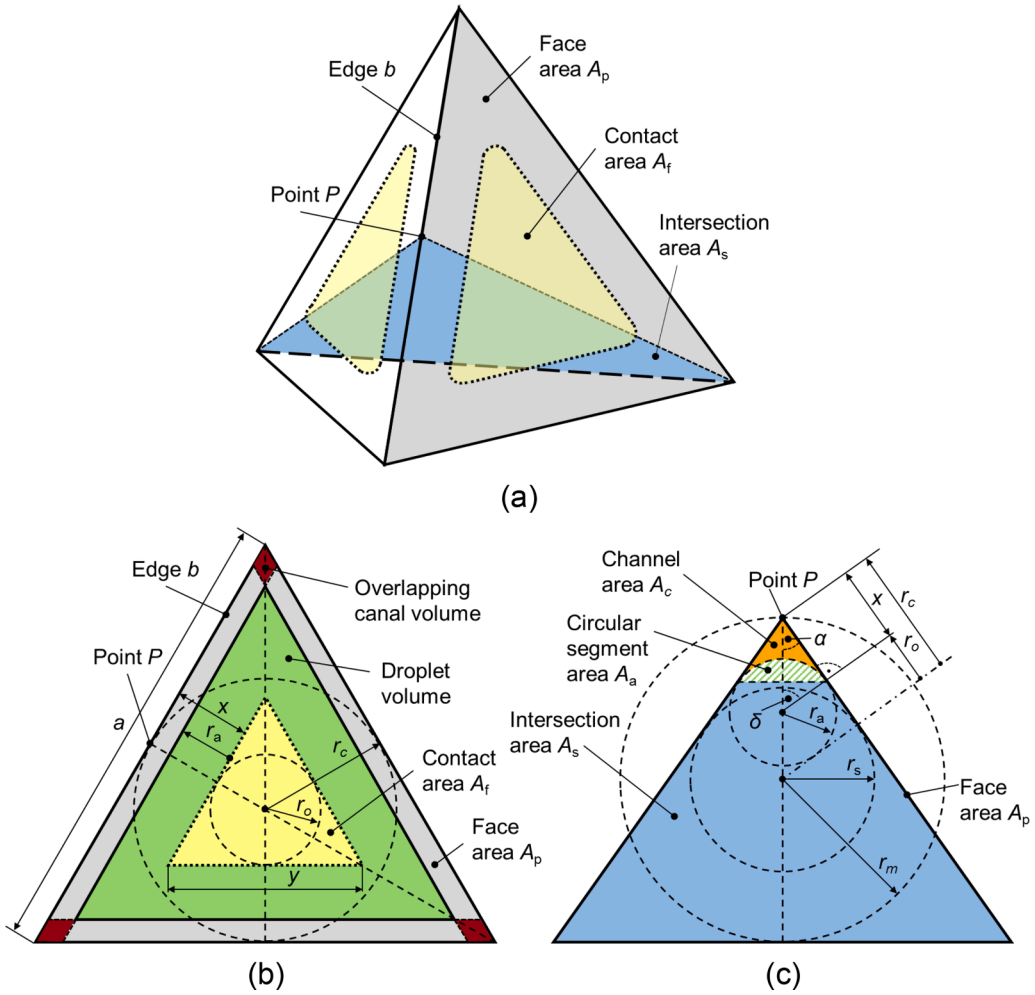

Fig. 2. Geometric relationship between the contact area radius r_f, the curvature radius r_a and the polyhedron edge length a, exemplified by the tetrahedron shape.

The channel volume is approximated according to Eq. (20), where A_c is the channel area and C_{cor} is a correction factor.

$$V_c = C_{cor} a A_c \tag{20}$$

The channel area $A_c = A_t - A_a$ (orange area in Fig. 2c) is the difference between the area A_t of an isosceles triangle with side length x and angle 2α, and the area A_a of the circular segment (hashed green area in Fig. 2c). The areas A_t and A_a are determined by Eqs. (21) and (22), respectively, where δ is located in the same right-angled triangle as α and is determined by $\delta = \pi/2 - \alpha$. In Eq. (22), δ is inserted in radiant.

$$A_t = \frac{x^2 \sin(2\alpha)}{2} = \left(\frac{r_a}{\tan(\alpha)}\right)^2 \frac{\sin(2\alpha)}{2} \tag{21}$$

$$A_a = \frac{r_a^2(2\delta - \sin(2\delta))}{2} \tag{22}$$

The correction factor C_{cor} is required because the channels overlap (red area in Fig. 2b), leading to an overestimation of the channel volume by Eq. (20) in the absence of this factor. To determine the correction factor, Eqs. (18)–(21) are considered at the boundary condition $p \to 0$. At this deformation state, the radius r of the undeformed droplet approaches the radius $r_s = C_{rs} a$ of the polyhedron's insphere, and $r_a \to r = r_s$. Therefore, the correction factor C_{cor} is derived according to Eq. (23) with α given by Eq. (16).

$$C_{cor} = \frac{2\left(C_V - \frac{4\pi}{3} C_{rs}^3\right)}{N_e C_{rs}^2 \left(\frac{\sin(2\alpha)}{\tan^2(\alpha)} - (\pi - 2\alpha - \sin(2\alpha))\right)} \tag{23}$$

Combining the introduced equations the general volumetric relationship is represented by Eq. (24). The resulting volumetric relationship is similar to the relationship proposed by Henschke (1995). However, the channel area is derived more precisely and the required relationships are derived in a general form in this work.

$$\frac{\pi}{6} d^3 = C_V a^3 - \frac{C_{cor} N_e}{2} \left(\frac{\sin(2\alpha)}{\tan^2(\alpha)} - (\pi - 2\alpha - \sin(2\alpha))\right) a r_a^2 \tag{24}$$

3.4. Boundary conditions and initial values

Before solving the equation system, boundary conditions for the parameters r_f, r_a, and a are defined. If a boundary condition equals zero, 10^{-9} is used instead of 0 to avoid numerical issues.

When the pressure $p \to 0$, the radii r_f and r_a approach their boundary conditions: $r_{f,min} = 0$ and $r_{a,max} = r$. Moreover, the radius of the undeformed droplet is equal to the radius r_s of the polyhedron's insphere at this state ($r = r_s = C_{rs} a$), resulting in $a_{max} = r/C_{rs}$.

When the pressure $p \to \infty$, the radius r_a approaches its boundary conditions: $r_{a,min} = 0$. In addition, at this pressure the area $A_f \to A_p$ resulting in $r_{f,max} = a_{min}\left(\frac{C_A}{\pi}\right)^{1/2}$ (Eq. (3) and Eq. (2)). Moreover, the polyhedron volume $V_p = C_V a^3$ is equal to the droplets volume $V = \frac{4\pi}{3} r$ at this condition, resulting in $a_{min} = \left(\frac{4\pi}{3C_V}\right)^{1/3} r$.

Based on these considerations the boundary conditions for r_f, r_a, and a are defined according to Eqs. (25), (26), and (27), respectively.

$$10^{-9} \le r_f \le \left(\frac{C_A}{\pi}\right)^{1/2} \left(\frac{4\pi}{3C_V}\right)^{1/3} r \tag{25}$$

$$10^{-9} \leq r_a \leq r \tag{26}$$

$$\left(\frac{4\pi}{3C_V}\right)^{1/3} r \leq a \leq \frac{r}{C_{rs}} \tag{27}$$

The initial guess values are defined according to Eqs. (28)–(30) with minimum and maximum values from the boundary conditions according to Eqs. (25)–(27).

$$a_0 = a_{min} + (a_{max} - a_{min})/2 \tag{28}$$

$$r_{a,0} = (r_{a,max} - r_{a,min})/2 \tag{29}$$

$$r_{f,0} = C_{rc} a_0/2 \tag{30}$$

3.5. Volume ratio

The volume ratio between the droplet's original volume and the volume of its corresponding polyhedral shape is determined according to Eq. (31).

$$\varepsilon_i = \frac{V}{V_p} = \frac{\pi}{6C_V}\left(\frac{d}{a}\right)^3 \tag{31}$$

Considering the boundary conditions introduced in Ch. 3.4, $a \to a_{max} = r/C_{rs}$, when the pressure $p \to 0$, resulting in $\varepsilon_i \to \varepsilon_{i,min}$ according to Eq. (32). When the pressure $p \to \infty$, $\varepsilon_i \to \varepsilon_{i,max} = 1$.

$$\varepsilon_{i,min} = \frac{4\pi C_{rs}^3}{3C_V} \tag{32}$$

3.6. Model application to polydisperse systems

The presented modeling approach is derived for a single droplet i with radius r. Therefore, r_f and r_a, as described in Ch. 3.1–3.4, represent the deformation characteristic radii for this single droplet or a monodisperse droplet size distribution. However, to calculate the coalescence between two droplets in a polydisperse droplet size distribution using Henschke's coalescence model (Henschke, 1995, 2002), r_f and r_a cannot be determined based on r. Coalescence is a binary phenomenon that occurs between a droplet pair, and the droplet radii can differ in polydisperse droplet size distributions. Therefore, instead of r, an equivalent droplet radius r_{eq}, as given by Eq. (33) (Abid and Chesters, 1994), is used to calculate r_f and r_a using the approach presented in this work (Ch. 3.1–3.4). In Eq. (33), r_1 and r_2 represent the radii of droplet one and droplet two, respectively.

$$r_{eq} = \frac{2}{\frac{1}{r_1} + \frac{1}{r_2}} \tag{33}$$

Moreover, instead of h and p, h_{eq} and p_{eq} are used as equivalent DPZ height and pressure acting on the droplet pair. Therefore, h_{eq} and p_{eq} are considered in the center between two droplets instead of at the droplet's center.

In contrast, ε_i is determined for each individual droplet. To explicitly distinguish between a droplet pair and an individual droplet in this study, r_i, h_i, and p_i are used instead of r, h, and p when referring to an individual droplet.

3.7. Bond number correlation

The iterative solution of the equation system is a time-consuming task, especially when used to simulate the droplet deformation in a DPZ of thousands of droplets over a long period. Therefore, the Bo number correlations proposed by Henschke (1995) are used as a quick calculation approach.

The Bo number is defined by Eq. (34) and the pressure p is calculated according to Eq. (1) with $p = p_{eq}$ and $d = d_{eq}$ used for determining r_f and r_a and $p = p_i$ and $d = d_i$ used for determining ε_i.

$$Bo = \frac{pd}{\sigma} \tag{34}$$

In contrast to the Bo number expression proposed by Henschke (1995), the pressure in Eq. (34) considers $\bar{\varepsilon}_p$ (Eq. (1)). This consideration is reasonable because only the dispersed phase within the DPZ is responsible for the deformation of the droplets and not the bulk phase (Ch. 3.1). The bulk phase only participates in the hydrostatic pressure p_h. Moreover, since the equation system (Ch. 3.1–3.3) considers the pressure according to Eq. (1), it is logical to include the same pressure for the correlation of r_f, r_a, and ε_i by the Bo number. Furthermore, Henschke reported an overestimation due to the Bo number correlation defined in his work (Henschke, 1995). Since the pressure according to Eq. (1) is lower than the pressure defined by Henschke (1995), the issue of overestimation is also faced by the pressure definition in this work.

Eqs. (35) and (36) (Henschke, 1995) represent the general form of the Bo number correlations for r_f and r_a, respectively, with $d_{eq} = 2r_{eq}$ as equivalent droplet diameter and C_j as fitting parameters determined for each polyhedral shape individually.

$$\frac{2r_f}{d_{eq}} = C_1\sqrt{1 - \frac{C_2}{Bo + C_2}} \tag{35}$$

$$\frac{2r_a}{d_{eq}} = 1 - \sqrt{1 - \frac{C_3}{Bo + C_3}} \tag{36}$$

The fitting parameter C_1 can be determined by considering the boundary conditions (Ch. 3.4) at $p_{eq} \to \infty$, where $Bo \to \infty$ and $r_f \to \left(\frac{C_A}{\pi}\right)^{1/2}\left(\frac{4\pi}{3C_V}\right)^{1/3} r_{eq}$ (Eq. (25)), resulting in $C_1 = \left(\frac{C_A}{\pi}\right)^{1/2}\left(\frac{4\pi}{3C_V}\right)^{1/3}$ and Eq. (37). The remaining fitting parameters are fitted to the results of the iterative solution of the equation system.

$$\frac{2r_f}{d_{eq}} = \left(\frac{C_A}{\pi}\right)^{1/2}\left(\frac{4\pi}{3C_V}\right)^{1/3}\sqrt{1 - \frac{C_2}{Bo + C_2}} \tag{37}$$

The Bo number correlation for ε_i is determined based on the results of the iterative solution. Moreover, generalized Bo number correlations with fitting parameters independent of the polyhedral shape are determined. Assuming the relationship between r_a, r_f, ε_i, and the Bo number holds for both regular and irregular convex polyhedral shapes with uniform a (Ch. 3), these correlations can approximate r_a, r_f, and ε_i for irregular convex polyhedral shapes.

Since all influencing parameters besides the polyhedral shape parameters are included in the Bo number, no dimensional analysis is performed to identify the suitable parameters for the generalization of the Bo number correlations. Instead, the values of the fitting parameters are compared to the polyhedral shape parameters (SI Tab. 1) and appropriate polyhedral shape parameters for the generalization are identified based on their similarities.

In addition, only the following polyhedral shape parameters (SI Tab. 1) are considered for the generalization, as these are unambiguously defined: number of polyhedron faces N_f, number of polyhedron edges N_e, number of polyhedron corners N_c and number of polyhedron's face corners N_{fc}. Irregular convex polyhedral shapes with uniform a consist of different face shapes. Thus, polyhedral shape parameters such as A_p or r_o are not considered for the generalization, as these are not unique for some polyhedral shapes. The generalized Bo number correlations are fitted to all iterative solution results.

3.8. Parameter range

The deformation described by the presented model is dependent on the parameters d, σ and p, which is further determined by $\Delta\rho$, $\bar{\varepsilon}_p$, and h. The value ranges of these parameters are set to match the technical applications to investigate the model performance in a relevant range. The following ranges are identified: d = 150–1500 µm (Sibirtsev et al., 2024, 2025), σ = 2–50 mN/m (Henschke, 1995), $\Delta\rho$ = 30–350 kg/m³ (Henschke, 1995), $\bar{\varepsilon}_p$ = 0.55–1.0 (Henschke, 1995; Sibirtsev et al., 2025), h = 1–50 mm (Henschke, 1995), resulting in $p \approx$ 0.2–200 Pa.

The Bo number range results in $Bo \approx 0$–150 based on these parameter ranges. In technical applications at industrial scale, higher d and h can occur, resulting in even higher Bo values. However, it is unnecessary to consider these high values when investigating the model since Henschke (1995) showed that at $Bo \approx 50$, the droplet deformation almost reaches its final deformation stage. At this stage, r_a and r_f reach their limit values, which are $r_a \to 0$ and $r_f \to r_{f,max}$. Increasing the Bo number further does not significantly affect r_a and r_f from this deformation stage onwards.

3.9. Iterative solution of the equation system and fitting procedure

With Eqs. (10), (17) and (24), the unknown parameters r_f, r_a and a, the set parameters d, σ, and p, as well as the polyhedral shape-dependent constants C_p (SI Tab. 1), the equation system is fully defined. A publicly accessible Python code (Sibirtsev, 2025) is used to solve the equation and to fit the Bo correlation parameters. The equation system is solved within the specified d, σ, and p ranges (Ch. 3.8). Each range is divided into ten steps. Thus, the equation system is solved at 1000 points for each polyhedral shape, resulting in 5000 simulations. For the solution of the equations system, the *scipy.optimize.minimize()* method (Virtanen et al., 2020) is used. Moreover, the *Nelder-Mead* solver (Virtanen et al., 2020) is used at $Bo \leq 1$ and the *Powell* solver (Virtanen et al., 2020) at $Bo > 1$, since it delivers the most accurate results in this work. The mean absolute percentage error (MAPE) according to Eq. (38) is used as minimization function, where $E_{L,j}$ and $E_{R,j}$ are the results of the left and the right hand side of the $N_E = 3$ equations, Eqs. (10), (17), and (24). Solutions with a $MAPE_1$ value higher than 1 % are excluded from further consideration.

$$MAPE_1 = 100 \frac{1}{N_E} \sum_{j=1}^{N_E} \left| \frac{E_{L,j} - E_{R,j}}{E_{L,j}} \right| \tag{38}$$

The results of the iterative solution of r_f, r_a and ε are not equally distributed over the Bo number range. Therefore, the Bo number values are transformed into a logarithmic scale to achieve a more even distribution of the data. Moreover, equally spaced bins within the transformed Bo number range are defined, and an equal number of randomly chosen iterative solution results within these bins is used to fit the Bo number correlation parameters. In this manner, a similar accuracy of the Bo number correlation is given over the entire range of the Bo number. For the fitting, the *Sequential Least Squares Programming (SLSQP)* solver of the *scipy.optimize.minimize()* method (Virtanen et al., 2020) is used since it is a fast solver and provides accurate results in this case. The MAPE, according to Eq. (39) is used as a minimization function for the fit, where N_p is the number of fitted points, A_j are the results of the iterative solution, and P_j are the predicted values by the Bo number correlation. In addition, the $MAPE_3$ is considered to make a statement about how accurate the fit is across all the simulations performed in this work. The $MAPE_3$ is equally defined as $MAPE_2$ (Eq. (39)) but takes all the results N_r of the iterative solution into account instead of N_p.

$$MAPE_2 = 100 \frac{1}{N_p} \sum_{j=1}^{N_p} \left| \frac{A_j - P_j}{A_j} \right| \tag{39}$$

All simulations are performed on an Intel Core i7-3740QM CPU.

4. Results & discussion

From 5000 simulations, approx. 29 % solutions of the equation system result in an $MAPE_1$ (Eq. (38)) over 1 %, and thus, are excluded from further consideration. The most of the results with $MAPE_1 > 1$ % are achieved at low p values. At these conditions, the Bo number values are low, which means that r_f is approaching its limit value of zero. One assumption is that it is difficult to achieve convergence in this area due to the strong gradient in the courses of r_f and r_a.

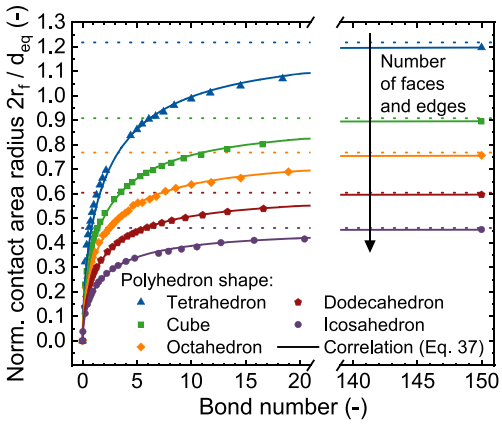

Fig. 3. Dependency of the normalized contact area radius $2r_f/d_{eq}$ on the Bo number for iterative solution results (points) and Bo number correlation (solid lines).

All equation system solutions with $MAPE_1 \leq 1$ % are used to investigate the dependency of r_f, r_a and ε_i on the Bo number and to fit the fitting parameters of the Eqs. (37) and (36). The resulting fitting parameters can be found in SI Tab. 2. For clarity, only every 25th point of the simulations is shown in the following graphs.

4.1. Contact area radius r_f

Fig. 3 shows the normalized contact area radius $2r_f/d_{eq}$ in dependence on the Bo number for iterative solution results (points) and Bo number correlation Eq. (37) (solid lines). The $2r_f/d_{eq}$ increases with increasing Bo number. The slope of the curves is steep at the beginning and decreases with an increase in the Bo number, whereby the course approaches a limit value (dotted lines). The observed change in the slope is because the contact area A_f is increasing linearly proportional with an increase in p_i or a decrease in σ (Eqs. (3) and (10)), and thus, an increase in the Bo number (Eq. (34)). Since r_f is proportional to the square root of A_f, the course follows a square root function as also shown by Henschke (1995). The correlation Eq. (37) matches this curve progression accurately with an $MAPE_2$ of 1.7 % and an $MAPE_3$ of 2.9 % averaged over the five polyhedral shapes.

Moreover, the limit value of $2r_f/d_{eq}$ is dependent on the polyhedral shape and decreases with the number of polyhedron faces and edges for a constant Bo number. Since the area potentially available as the droplet contact area A_f decreases with the number of faces, and thus, decreasing polyhedron face area A_p, the limit value of $2r_f/d_{eq}$ also decreases. For the dodecahedron, a limit value of approx. 0.6 is reached in this work. This value is also reached by the deformation modeling performed by Henschke (1995).

4.2. Curvature radius r_a

Fig. 4a shows the normalized curvature radius $2r_a/d_{eq}$ in dependence on the Bo number for iterative solution results (points) and the Bo number correlation Eq. (36) (solid lines). The radius $2r_a/d_{eq}$ decreases with an increasing Bo number. The slope of the curves is steep at the beginning and decreases with the increase in the Bo number, whereby the course approaches a limit value of zero. The observed change in the slope is because r_a is decreasing almost linearly anti-proportional with an increase in p_i or a decrease in σ (Eq. (10)), and thus, an increase in the Bo number.

Moreover, $2r_a/d_{eq}$ is dependent on the polyhedral shape and increases with the number of polyhedron edges for a constant Bo number. One possible explanation is that the total deformation of a droplet is distributed over all curvature regions of the polyhedron. The more edges a polyhedron has, the higher its number of curvature regions, and

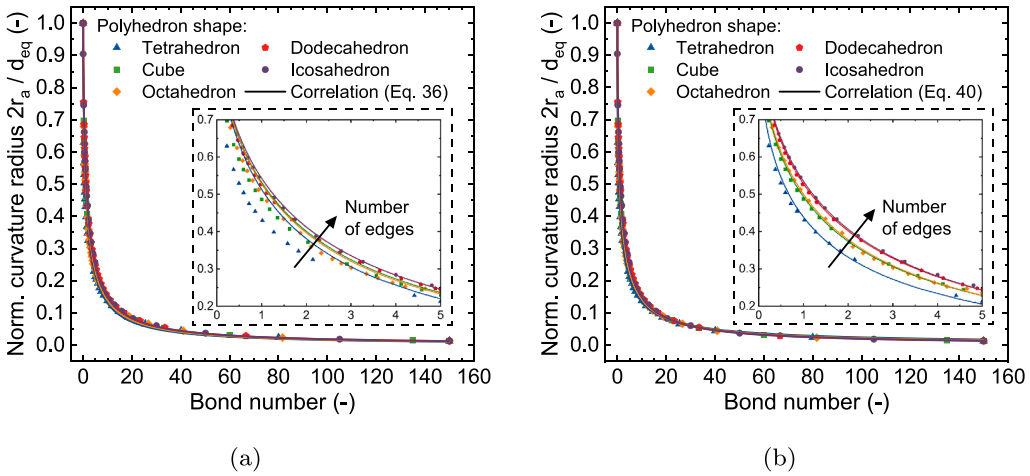

Fig. 4. Dependency of the normalized contact area radius $2r_a/d_{eq}$ on the Bo number for iterative solution results (points) and Bo number correlation (solid lines) according to (a) Eq. (36) and (b) Eq. (40).

the less the deformation in each curvature region, resulting in higher r_a values. Therefore, at the same Bo numbers and thus the same degree of deformation, a polyhedral shape with a higher number of edges has a higher $2r_a/d_{eq}$ value than one with a lower number of edges.

Even though the Bo number correlation Eq. (36) matches the curve progression with an $MAPE_2$ of 5.5 % and an $MAPE_3$ of 5.3 % averaged over the five polyhedral shapes, it overestimates the $2r_a/d_{eq}$ values in the range of $Bo = 0.2 \dots 4.5$. This overestimation is also noticed for the dodecahedron shape by Henschke (1995). It is assumed that one fitting parameter (C_3) cannot accurately describe the curve progression by the Bo number correlation. Therefore, a second fitting parameter is introduced resulting in Eq. (40), with C_4 and C_5 as the fitting parameters. The parameter C_5 is chosen because it allows the adjustment of the slope of the asymptotic curve progression.

$$\frac{2r_a}{d_{eq}} = 1 - \sqrt{1 - \frac{C_4}{Bo^{C_5} + C_4}} \tag{40}$$

Fig. 4b shows the $2r_a/d_{eq}$ in dependence on the Bo number according to Eq. (40). The correlation Eq. (40) matches the curve progression in the range of $Bo = 0.2 \dots 4.5$ more accurately with an $MAPE_2$ and an $MAPE_3$ of 2.0 % averaged over the five polyhedral shapes.

4.3. Volume ratio ε_i

Fig. 5 shows the volume ratio ε_i in dependence on the Bo number for iterative solution results (points) and Bo number correlation (solid lines). The ε_i increases with increasing Bo number, starting at $\varepsilon_i(Bo = 0) = \varepsilon_{i,\min}$ and asymptotically approaching $\varepsilon_i(Bo \to \infty) = \varepsilon_{i,\max}$ (Ch. 3.5. The slope of the curves is steep at the beginning and decreases with an increase in the Bo number, whereby the course approaches a limit value of $\varepsilon_{i,\max} = 1$. The observed change in the slope occurs because the square of the edge length a^2, increases linearly with an increase in p_i or a decrease in σ (Eq. (10)), and thus, an increase in the Bo number (Eq. (34)). As a result, a follows a square root dependence on Bo.

Moreover, ε_i depends on the polyhedral shape and increases with the number of polyhedron faces and edges for a constant Bo number. One explanation for this observation is that the polyhedral shape approaches a spherical shape with an increasing number of faces and edges. By approaching the spherical shape, the volume in the channels between the droplets decreases and the volume ratio ε_i approaches 1.

The observed curve progression can be described by Eq. (41). The fitting parameter C_6 can be determined by considering the boundary conditions (Ch. 3.4) at $p_i \to 0$, where $Bo \to 0$ and $\varepsilon_i \to \varepsilon_{i,\min} = \frac{4\pi C_{rs}^3}{3C_V}$ (Eq. (32)), resulting in $C_6 = \frac{4\pi C_{rs}^3}{3C_V}$ and Eq. (42). The fitting parameter

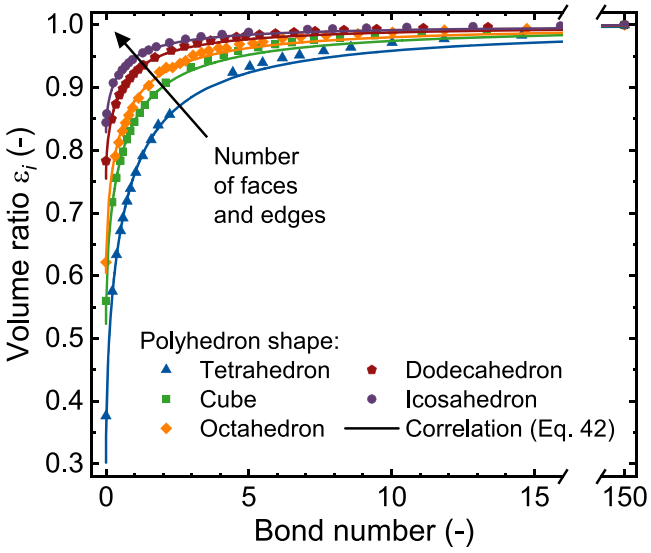

Fig. 5. Dependence of the volume ratio ε_i on the Bo number for iterative solution results (points) and Bo number correlation (solid line).

C_7 is fitted to the results of the iterative solution (SI Tab. 2). The correlation Eq. (42) matches the curve progression accurately with an $MAPE_2$ and an $MAPE_3$ of 0.6 % averaged over the five polyhedral shapes. However, at $Bo > 2$ Eq. (41) slightly underestimates ε_i.

$$\varepsilon_i = C_6 + (1 - C_6)\sqrt{1 - \frac{C_7}{Bo + C_7}} \tag{41}$$

$$\varepsilon_i = \frac{4\pi C_{rs}^3}{3C_V} + \left(1 - \frac{4\pi C_{rs}^3}{3C_V}\right)\sqrt{1 - \frac{C_7}{Bo + C_7}} \tag{42}$$

4.4. Generalization of the Bond number correlations

After comparing the polyhedral shape dependent fitting parameters C_j (SI Tab. 2) with the geometrical parameters of the polyhedral shapes (SI Tab. 1), N_f and N_e are chosen to generalize Eqs. (35), (36), and (41) to (43), (44), and (45) with polyhedral shape independent fitting parameters. Since irregular convex polyhedral shapes with uniform a consist of different face shapes, $\bar{r}_f$ and $\bar{r}_a$ are considered as the average contact area radius and the average radius of droplet's curvature regions,

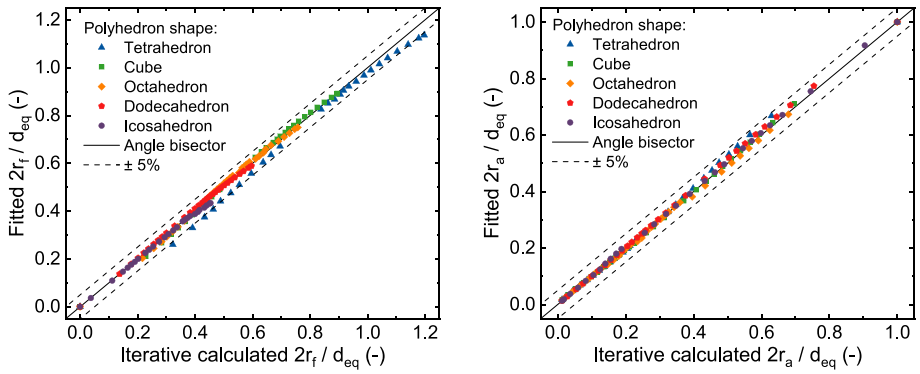

Fig. 6. Comparison between iterative determined (Eqs. (10), (17) and (24)) and fitted (a) (Eq. (43)) $2r_f/d_{eq}$ and (b) (Eq. (44)) $2r_a/d_{eq}$ values.

respectively.

$$\frac{2\bar{r}_f}{d_{eq}} = \frac{2.65}{N_f^{0.6}}\sqrt{1-\frac{5.0/N_e^{0.1}}{Bo+5.0/N_e^{0.1}}} \tag{43}$$

$$\frac{2\bar{r}_a}{d_{eq}} = 1-\sqrt{1-\frac{1.35N_e^{0.3}}{Bo^{\left(0.7N_e^{0.1}\right)}+1.35N_e^{0.3}}} \tag{44}$$

$$\begin{aligned}\varepsilon_i &= \Psi+(1-\Psi)\sqrt{1-\frac{1.41N_e^{0.1}}{Bo+1.41N_e^{0.1}}}\\ \Psi &= -8.13+(1+8.13)\sqrt{1-\frac{0.714}{N_f+0.714}}\end{aligned} \tag{45}$$

The choice of N_f in Eq. (43) is based on the consistent opposing behavior observed between N_f and C_1 when the polyhedral shape changes (Fig. 3). The significant influence of N_f on r_f is logical, as for the same Bo numbers and d_{eq}, polyhedra with a higher number of faces have smaller contact areas A_f and thus lower r_f values (Ch. 4.1). In contrast, C_2 correlates most accurately with N_e. However, N_e has a smaller influence on r_f in Eq. (43) compared to N_f.

The choice of N_e in Eq. (44) is based on the consistent similar behavior observed between N_e, C_4, and C_5 when the polyhedral shape changes (Fig. 4). The significant influence of N_e on r_a is logical, as for the same Bo numbers and d_{eq}, a larger curvature radius r_a is expected for polyhedra with a higher number of edges (Ch. 4.2).

The choice of N_e and N_f in Eq. (45) is based on the consistent similar behavior observed between N_e and C_6, and the opposing behavior observed between N_f and C_7 when the polyhedral shape changes (Fig. 5). The influence of N_e and N_f on ε_i is logical, as for the same Bo numbers and d_i, the polyhedral shape approaches a spherical shape with an increasing number of faces, leading to an increase in ε_i (Ch. 4.3).

Fig. 6 and SI Fig. 7 show the comparison between iterative determined (Eqs. (10), (17), (24), and (31)) and fitted (Eqs. (43), (44), and Eq. (45)) $2\bar{r}_f/d_{eq}$, $2\bar{r}_f/d_{eq}$, and $\bar{\varepsilon}_i$ values. The generalized Bo number correlations show high accuracies with $MAPE_2$ of 2.3 %, 2.4 %, and 0.6 % and $MAPE_3$ of 2.8 %, 2.4 % and 0.6 % for Eqs. (43), (44), and (45), respectively. All $2r_f/d_{eq}$, $2r_f/d_{eq}$, and ε_i values are located within an interval of ±5 %. Only for the tetrahedron shape $2r_f/d_{eq}$ falls below the interval of ±5 % at $2r_f/d_{eq} < 0.6$.

Since Eqs. (43), (44), and (45) incorporate the polyhedral shape parameters, N_f and N_e, the presented Bo number correlations can be utilized not only to predict r_f, r_a, ε_i for regular polyhedral shapes but also to estimate these parameters for irregular convex polyhedral shapes with uniform a. The specific polyhedral shape adopted by a droplet in the DPZ can be determined using the simulation method outlined by Sibirtsev et al. (2025). This method calculates the contact number of the droplet within the DPZ, identifying N_f as the contact number. The parameter N_e is subsequently determined based on the identified polyhedral shape.

5. Conclusion

This study presents a novel modeling approach to characterize droplet deformation into polyhedral shapes within liquid-liquid polydisperse dense-packed zones (DPZs). The deformation is described by two characteristic radii: the contact radius r_f and the curvature radius r_a, as well as the volume ration ε_i. These parameters are determined through a system of equations based on pressure, geometric, and volumetric relationships for regular polyhedra. Additionally, generalized correlations based on the Bond (Bo) number are introduced to predict droplet deformation for regular polyhedral shapes and to estimate droplet deformation for irregular convex polyhedral shapes. The droplet deformation is simulated across a Bo number range relevant to technical applications.

The simulation results reveal that the contact radius r_f increases with increasing Bo number and decreasing numbers of polyhedron faces and edges, approaching a shape-dependent limit. Conversely, the curvature radius r_a exhibits the opposite trend, decreasing as Bo numbers increase and approaching a zero-limit at high Bo number values. The volume ratio ε_i increases with increasing Bo number and numbers of polyhedron faces and edges, approaching the limit-value of 1. The generalized Bo number correlations strongly agree with the equation system solutions, achieving mean absolute percentage errors below 3.0 % and an average deviation of less than ±5 %.

The findings on droplet deformation into polyhedral shapes provide valuable practical implications. These insights can be applied to predict droplet deformation in liquid-liquid polydisperse DPZs, enhancing the utility and relevance of this research. Furthermore, the proposed modeling approach facilitates seamless integration into Henschke's coalescence model (Henschke, 1995, 2002), as this model uses the same characteristic radii r_f and r_a.

In future work, the deformation model will be implemented in a simulation environment to simulate the formation and dissolution of DPZs during the phase separation of polydisperse liquid-liquid dispersions. Furthermore, the validity of the proposed Bo number correlations for irregular convex polyhedral shapes will be verified by adapting and solving the introduced equation system for such geometries. In addition, the presented modeling approach will be validated by experimental investigations.

Data availability

The link to the Python source code of this work can be found on GitLab (Sibirtsev, 2025).

Declaration of competing interest

The authors declare that they have no known competing financial interests or personal relationships that could have appeared to influence the work reported in this paper.

CRediT authorship contribution statement

Stepan Sibirtsev: Writing – original draft, Visualization, Software, Project administration, Methodology, Investigation, Data curation, Conceptualization; **Lukas Thiel:** Writing – review & editing; **Yannik Danner:** Writing – review & editing, Methodology, Investigation; **Andrey Kirsanov:** Writing – review & editing, Methodology, Investigation; **Andreas Jupke:** Writing – review & editing, Supervision, Resources

Supplementary material

Supplementary material associated with this article can be found in the online version at 10.1016/j.ces.2025.121575

References

Abe, K., Inasawa, S., 2022. Deformation and coalescence of particle-stabilized oil droplets in drying aqueous NaCl solutions. Colloids Surf. A 632, 127816. https://doi.org/10.1016/j.colsurfa.2021.127816

Abid, S., Chesters, A.K., 1994. The drainage and rupture of partially-mobile films between colliding drops at constant approach velocity. Int. J. Multiphase Flow 20 (3), 613–629. https://doi.org/10.1016/0301-9322(94)90033-7

Bozzano, G., Dente, M., 2010. Mechanism of drop coalescence at the interface of two immiscible liquids. In: 20th European Symposium on Computer Aided Process Engineering. Elsevier. Vol. 28 of *Computer Aided Chemical Engineering*, pp. 55–60. https://doi.org/10.1016/S1570-7946(10)28010-0

Bronshteĭn, I.N., 2007. Handbook of Mathematics. Springer, Berlin and New York. 5th ed. edition.

Chan, D. Y.C., Klaseboer, E., Manica, R., 2011. Film drainage and coalescence between deformable drops and bubbles. Soft Matter 7 (6), 2235–2264. https://doi.org/10.1039/C0SM00812E

Chen, J.-D., Hahn, P.S., Slattery, J.C., 1984. Coalescence time for a small drop or bubble at a fluid–fluid interface. AlChE J. 30 (4), 622–630. https://doi.org/10.1002/aic.690300413

de Gennes, P.-G., Brochard-Wyart, F., Quéré, D., 2004. Capillarity and wetting phenomena: Drops, bubbles, pearls, waves. Springer, New York.

Dunne, F.F., Winkelmann, J., Weaire, D., Hutzler, S., 2019. Implementation of Morse–Witten theory for a polydisperse wet 2D foam simulation. Philos. Mag. 99 (18), 2303–2320. https://doi.org/10.1080/14786435.2019.1624852

Eberz, J., Sibirtsev, S., Jupke, A., 2025. Mini-batch settling cell for investigation of liquid-liquid phase separation. Chem. Eng. Sci. 301, 120751. https://doi.org/10.1016/j.ces.2024.120751

Eggert, A., Kögl, T., Arlt, W., Jupke, A., 2019. Computer tomographic detection of the liquid–liquid mixing and separation within the annular centrifugal contactor/extractor. Chem. Eng. Res. Des. 142, 143–153. https://doi.org/10.1016/j.cherd.2018.11.034

Frising, T., Noïk, C., Dalmazzone, C., 2006. The liquid/liquid sedimentation process: from droplet coalescence to technologically enhanced water/oil emulsion gravity separators: a review. J. Dispers. Sci. Technol. 27 (7), 1035–1057. https://doi.org/10.1080/01932690600767098

Graham, E.E., Ooi, K.L., Odell, M.H., 1979. Drop size distributions for non-coalescing liquid—liquid systems in sieve plate columns. The Chemical Engineering Journal 18 (3), 189–196. https://doi.org/10.1016/0300-9467(79)80117-3

Henschke, M., 1995. Dimensionierung liegender Flüssig-flüssig-Abscheider anhand diskontinuierlicher Absetzversuche. Vol. Nr. 379 of *Fortschritt-Berichte VDI. Reihe 3, Verfahrenstechnik*. VDI Verlag, Düsseldorf.

Henschke, M., 2002. Determination of a coalescence parameter from batch-settling experiments. Chem. Eng. J. 85 (2–3), 369–378. https://doi.org/10.1016/S1385-8947(01)00251-0

Höhler, R., Weaire, D., 2019. Can liquid foams and emulsions be modeled as packings of soft elastic particles? Adv. Colloid Interface Sci. 263, 19–37. https://doi.org/10.1016/j.cis.2018.11.002

Lacasse, M.D., Grest, G.S., Levine, D., 1996. Deformation of small compressed droplets. Phys. Rev. E Stat. Phys. Plasmas Fluids Relat. Interdiscip. Top. 54 (5), 5436–5446. https://doi.org/10.1103/PhysRevE.54.5436

Leleu, D., Pfennig, A., 2019. Coalescence modeling for design of technical equipment. Chem. Eng. Technol. 42 (7), 1404–1413. https://doi.org/10.1002/ceat.201900037

Liu, W., Chen, S., Wu, C.-Y., Li, S., 2019. Unified size-density and size-topology relations in random packings of dry adhesive polydisperse spheres. Phys. Rev. E 99 (2-1), 022901. https://doi.org/10.1103/PhysRevE.99.022901

Mohanty, S., Vogelpohl, A., 1997. A simplified hydrodynamic model for a pulsed sieve-plate extraction column. Chem. Eng. Process. 36 (5), 385–395. https://doi.org/10.1016/S0255-2701(97)00010-X

Morse, D.C., Witten, T.A., 1993. Droplet elasticity in weakly compressed emulsions. Europhys. Lett. (EPL) 22 (7), 549–555. https://doi.org/10.1209/0295-5075/22/7/012

Raynel, G., Marques, D.S., Al-Thabet, M., 2023. The influence of water droplet packing on crude oil emulsion. Eur. Phys. J. E Soft Matter 46 (7), 53. https://doi.org/10.1140/epje/s10189-023-00311-9

Rommel, W., Meon, W., Blass, E., 1992. Hydrodynamic modeling of droplet coalescence at liquid-liquid interfaces. Sep. Sci. Technol. 27 (2), 129–159. https://doi.org/10.1080/01496399208018870

Schlieper, L., Chatterjee, M., Henschke, M., Pfennig, A., 2004. Liquid-liquid phase separation in gravity settler with inclined plates. AlChE J. 50 (4), 802–811. https://doi.org/10.1002/aic.10075

Sibirtsev, S., 2025. Droplet deformation GitLab repository. https://git.rwth-aachen.de/avt-fvt/public/droplet-deformation. Access date: 2025-01-11.

Sibirtsev, S., Göbel, C.B., Jupke, A., 2019. Automation of a procedure for the experimental investigation of liquid–liquid phase separation. Chem. Ing. Tech. 91 (12), 1787–1793. https://doi.org/10.1002/cite.201900162

Sibirtsev, S., Thiel, L., Kirsanov, A., Jupke, A., 2025. Droplet contact numbers and contact probabilities in liquid–liquid dense–packed zones. AlChE J. https://doi.org/10.1002/aic.18723

Sibirtsev, S., Thiel, L., Zhai, S., Recke, L., Cai, Y.T., Jupke, A., 2024. Experimental and model-based investigation of the droplet size distribution during the mixing process in a batch-settling cell. Can. J. Chem. Eng.. Manuscript under review (revision 1)

Sovilj, M.N., Nikolovski, B.G., Spasojević, M.D., 2019. Hydrodynamics in spray and packed liquid-liquid extraction columns: a review. M top Maced. J. Chem. Chem. Eng. 38 (2), 267. https://doi.org/10.20450/mjcce.2019.1519

Steinhoff, J., Charlafti, E., Leleu, D., Reinecke, L., Franken, H., Becker, K., Kalem, M., Sixt, M., Braß, M., Borchardt, D., Bäcker, W., Wegener, M., Maaß, S., Weber, M., Acher, T., Matten, C., Pfennig, A., Kraume, M., Bart, H.-J., 2021. Energie– und ressourceneinsparung durch innovative und CFD–basierte auslegung von flüssig/flüssig–schwerkraftabscheidern. Chem. Ing. Tech. 93 (7), 1152–1165. https://doi.org/10.1002/cite.202000083

Steinhoff, J., Gebauer, F., Fölsch, D., Bart, H.-J., 2018. Optimized description of dispersion layers on a vertical separator. Chem. Ing. Tech. 90 (7), 979–987. https://doi.org/10.1002/cite.201700092

Thaker, A.H., Buwa, V.V., 2019. Experimental investigations of interfacial and binary coalescence of multilayered drops. Ind. Eng. Chem. Res. 58 (18), 7620–7632. https://doi.org/10.1021/acs.iecr.8b05994

Thaker, A.H., Darekar, M., Singh, K.K., Buwa, V.V., 2018. Experimental investigations of liquid–liquid disengagement in a continuous gravity settler. Chem. Eng. Res. Des. 139, 174–187. https://doi.org/10.1016/j.cherd.2018.09.031

Virtanen, P., Gommers, R., Oliphant, T.E., Haberland, M., Reddy, T., Cournapeau, D., Burovski, E., Peterson, P., Weckesser, W., Bright, J., van der Walt, S.J., Brett, M., Wilson, J., Millman, K.J., Mayorov, N., Nelson, A. R.J., Jones, E., Kern, R., Larson, E., Carey, C.J., Polat, İ., Feng, Y., Moore, E.W., VanderPlas, J., Laxalde, D., Perktold, J., Cimrman, R., Henriksen, I., Quintero, E.A., Harris, C.R., Archibald, A.M., Ribeiro, A.H., Pedregosa, F., van Mulbregt, P., 2020. Scipy 1.0: fundamental algorithms for scientific computing in python. Nat. Methods 17 (3), 261–272. https://doi.org/10.1038/s41592-019-0686-2

Weber, B., Jupke, A., 2020. Compartment–model for the simulation of the separation performance of stirred liquid–liquid–extraction columns. AlChE J. 66 (8). https://doi.org/10.1002/aic.16286

Ye, S., Hohl, L., Charlafti, E., Jin, Z., Kraume, M., 2023a. Effect of temperature on mixing and separation of stirred liquid/liquid dispersions over a wide range of dispersed phase fractions. Chem. Eng. Sci. 274, 118676. https://doi.org/10.1016/j.ces.2023.118676

Ye, S., Hohl, L., Kraume, M., 2023b. Impact of feeding conditions on continuous liquid-liquid gravity separation, Part I: inlet and outlet drop size, dense-packed zone and separation efficiency. Chem. Eng. Sci. 282, 119237. https://doi.org/10.1016/j.ces.2023.119237